Accelerated discovery of multi-property optimized Fe–Cu alloys

N.B. When citing this work, cite the original published paper.

(article starts on next page)

Accelerated discovery of multi-property optimized Fe–Cu alloys

X. Xu [a,b], Li Ping Tan [a], Karl P. Davidson [a], Shakti P. Padhy [a], V. Chaudhary [c,*],
R.V. Ramanujan [a,**]

[a] *School of Materials Science and Engineering, Nanyang Technological University, 639798, Singapore*
[b] *School of Materials Science and Engineering, Nanjing University of Science and Technology, Nanjing, 210094, China*
[c] *Industrial and Materials Science, Chalmers University of Technology, SE-41296, Gothenburg, Sweden*

ABSTRACT

The next generation of rotating electrical machines requires materials with an optimized combination of magnetic, electrical and mechanical properties. High-throughput experiments can accelerate the discovery of relevant materials. Past work has focused on complex multicomponent alloys in which it is difficult to pinpoint the effect of each component. On the other hand, in this work, Fe–Cu binary alloys were used as a model materials system to determine the feasibility of novel materials discovery through a rapid determination of multiple properties. The microstructures, magnetic, electrical, and mechanical properties of Fe–Cu alloys were rapidly determined. With increasing Cu content in Fe-xCu from 0 to 40 wt.%, the phases present changed from single phase BCC to a two-phase FCC + BCC microstructure. There was a decline in the saturation magnetization (M_s) from 211.3 to 118 emu/g. The hardness value increased from 166.3 HV to 238.5 HV, the coercivity (H_c) ranged from 14.6 to 45.7 Oe, and the resistivity varied between 27.3 and 43.0 μΩ·cm. The increased content of a Cu-rich phase led to a decrease in M_s and grain size, and higher H_c and hardness. Using an accelerated methodology, a significant variation in material properties was determined. Three compositions, i.e., Fe–3Cu, Fe–4Cu and Fe–10Cu, with a good balance of properties were identified for potential use in energy applications.

1. Introduction

Soft magnetic materials (SMM) are used in a plethora of applications such as electrical rotating machines, transformers, converters, actuators, recording heads and sensors etc. [1]. Increasingly, rotating electrical machines, e.g., motors, require operation at high frequencies, high speed and high torque. Hence, apart from good magnetic properties, superior electrical and mechanical properties are also essential to achieve improved efficiency and power density [2,3]. Hence, to identify novel materials compositions which can satisfy these requirements, the study of multiple properties is necessary.

Traditionally, new material discovery has relied on high cost, slow, trial-and-error approaches to study a small number of alloy compositions. The speed of research and development of new materials is very slow compared to the demand for improved material properties. With the advancement of artificial intelligence (AI) and inverse design, the rapid screening of multiple properties of a range of material compositions is required. Predictions derived from AI and machine learning (ML)

models [4] need to be validated by high-throughput (HT) techniques [5]. Combinatorial materials science [6], integrated computational materials science [7] and materials genome initiative [8] are some of the methods used for accelerating the development of novel materials. The combination of HT computing and design, HT characterization, material databases, and AI dramatically reduces material development cycles, lowers material development costs, and can quickly pinpoint new materials that meet performance requirements.

HT rapid experimental alloy development methods, incorporating computational work and machine learning, were deployed by Vecchio et al. [9] on nickel-based alloy systems with different compositions. Santodonato et al. [10] used HT thermodynamic calculations to predict the phase evolution of Al containing high entropy alloys (HEA). Yang et al. [11] used the high throughput CALPHAD method to revisit the valence electron concentration (VEC) rule in the AlCoCrFeNi HEA system. They proposed a data screening method to down-screen the candidate alloy compositions. Prior work on rapid HT SMM materials development, e.g., Padhy et al. [12], focused on the rapid

characterization and evaluation of Fe–Co–Ni alloys prepared by combinatorial flow synthesis and HT spark plasma sintering, and identified novel compositions with an attractive balance of multiple properties. The proof of concept was established in studies with smaller sample sizes, material libraries of the Fe–Co–Ni alloy system were prepared using different processing techniques [13,14]. Teh et al. [15] and Padhy et al. [16] prepared compositionally graded Fe–Co–Ni samples *via* laser engineered net shaping (LENS) and magnetron co-sputtering deposition, respectively.

A common strategy to improve mechanical, magnetic and electrical properties of SMM had been to focus on complex ternary, quaternary and HEA alloys [3,17–20]. For example, the microstructure, mechanical and magnetic properties of AlxCrCuFeNi$_2$ samples with a gradient composition prepared by HT laser deposition methods had been studied [21].

As the behaviour of these multi-element alloys are complex due to the large number of components, an understanding of the relative importance of each element was not possible. Hence, Fe–Cu was investigated as a simple model system in which we start with an element, Fe, which has good magnetic properties, but low electrical resistivity and mechanical strength. This leads to excessive eddy current losses and is incompatible for use in high speed and high torque applications. It is hypothesized that Cu can be used to increase the strength and resistivity without a large drop in magnetic properties. An accelerated approach was used to generate data to test our hypothesis.

Earlier reports on this material system focused more on Cu-rich compositions and a few Fe-rich compositions. The microstructure, magnetic, mechanical and electrical properties were separately investigated [22–25]. Apart from mechanical alloying [24], other synthesis routes which have been explored include chemical synthesis [26], deposition methods [22,27], additive manufacturing [28], gas atomization [29] and vacuum arc melting [30]. Mechanical alloying is used in this work as it is a non-equilibrium processing method which is attractive for processing normally immiscible alloys, such as Fe-Cu [31].

First, Fe-xCu alloys (where x in wt.% = 1 to 10 in intervals of 1 wt.%, and 15 to 40, in intervals of 5 wt.%) were prepared using a HT approach by ball milling and spark plasma sintering, and their magnetic, electrical and mechanical properties were determined. The significance of the work is the HT discovery of 3 novel compositions with a good multiple property set potentially relevant to next-generation electrical motors. Further detailed investigations can be conducted in the future into these compositions.

2. Materials and methods

2.1. Sample preparation

Elemental Fe (<195 μm, 99%) and Cu (<425 μm, 99.5%) powders from Sanvik Osprey and Sigma Aldrich, respectively, were mechanically alloyed in a high energy planetary ball mill (Fritsch Pulverisette 7 planetary micro mill). A total of 10 g of Fe and Cu powders were loaded with 10 mm diameter tungsten carbide balls in vials (with a ball-to-powder weight ratio of 10:1), and 0.5 mL of absolute ethanol was added to the powders as a control agent. Each cycle of milling (at 500 rpm) consisted of 10 min of milling time, followed by a pause of 10 min, to avoid overheating. The total milling time of the samples was 6 h. Each ball mill can hold 2 vials in each run; thus only 8 runs were required to prepare a total of 16 compositions (wt.% of Cu = 1, 2, 3, 4, 5, 6, 7, 8, 9, 10, 15, 20, 25, 30, 35 and 40).

HT spark plasma sintering (SPS) was carried out in a custom-made multicavity die, at a vacuum level <8 Pa, using Fuji Electronic Industrial, SPS-211LX. During the sintering process, the powder samples were compressed at a pressure of 40 MPa and sintered at a maximum temperature of 750 °C for 15 min. For each SPS run, 4 pellets of single compositions were prepared. This HT approach reduced the number of SPS runs by 75%. The samples were then vertically sliced, characterized

and their material properties evaluated. The density of the SPS samples were measured *via* the Archimedes method.

2.2. Accelerated phase identification and microstructural characterization

Phase identification of samples was done *via* X-ray diffraction (XRD) conducted at room temperature using a Bruker D8 Advance diffractometer, employing Cu Kα radiation (λ = 0.15405 nm) over a 2θ range of 20°–80°. The operating voltage and current were 40 kV and 40 mA, respectively. Equipped with a robotic arm, multiple samples could be loaded, and measurements can be set to be performed automatically. TOPAS V6 was used to calculate the phase fractions.

Electron microscopy studies and elemental mapping were performed on a JEOL JSM-7800F PRIME field emission scanning electron microscope (FESEM), with an attached Aztec – Ultim Max 170 mm^2 energy dispersive X-ray (EDX) spectrometer and a Symmetric electron backscatter diffraction (EBSD) detector. Maps were taken at an accelerating voltage of 20 kV and probe current of >30 nA. Grain size observation was performed *via* crystallographic texture maps obtained at a step size of 0.15 μm in EBSD, using the area-weighted mean values. Multiple samples could be mounted in conductive epoxy for ease of sample preparation and observations.

2.3. Material properties testing

The microhardness was measured at a load of 1 kgf using a Vickers hardness tester (Future-Tech). An automated four-point probe tester was used to determine the electrical resistivity of each composition. Magnetic characterization was performed on similarly sized samples using a Lakeshore 7400 vibrating sample magnetometer (VSM) for magnetic fields up to 14.5 kOe, calibrated with a Ni standard, while the Curie temperature for selected samples were determined using a thermogravimetric analysis (TGA, TA Instruments Q600 SDT) instrument and a permanent magnet, which is a method developed in-lab [14,32]. Calibration was also done prior to measurements, using Fe as a standard. Each cycle takes about 2.5 h to complete, compared to using traditional magnetization-temperature measurements, which can take a day to complete.

From the results obtained, the Pearson correlation factor (r) was calculated from the Equation (1) [33]:

$$r = \frac{\sum\limits_{i=1}^{n} (X_i - \overline{X})(Y_i - \overline{Y})}{\sqrt{\sum\limits_{i=1}^{n} (X_i - \overline{X})^2} \sqrt{\sum\limits_{i=1}^{n} (Y_i - \overline{Y})^2}} \qquad (1)$$

where r is the Pearson correlation factor, X_i and Y_i are the observed values of the two variables, and $\overline{X}$ and $\overline{Y}$ are the mean values of the two variables, respectively. This factor can be used to understand the relationship between composition and the material properties.

The Fe–Cu phase diagram [34], and an overview of the experimental process and characterization, is shown in Fig. 1. From the phase diagram Fig. 1(a), the solubility limit of Cu in Fe below 600°C is ~0.35%. Above this Cu content, Fe–Cu alloys can form new phases. Mechanical alloying can increase this solubility limit [31], as it is a solid-state processing technique. Fig. 1(b) presents the experimental processes and accelerated assessment of the alloys after mechanical alloying and SPS.

3. Results and discussion

3.1. Phase analysis using X-ray diffraction

Fig. 2(a) and (b) show the XRD patterns of the as ball milled Fe-xCu powders. For a Cu content of 1–4 wt.%, a single body-centered cubic (BCC) structure, identified by the 110 and 200 BCC diffraction peaks,
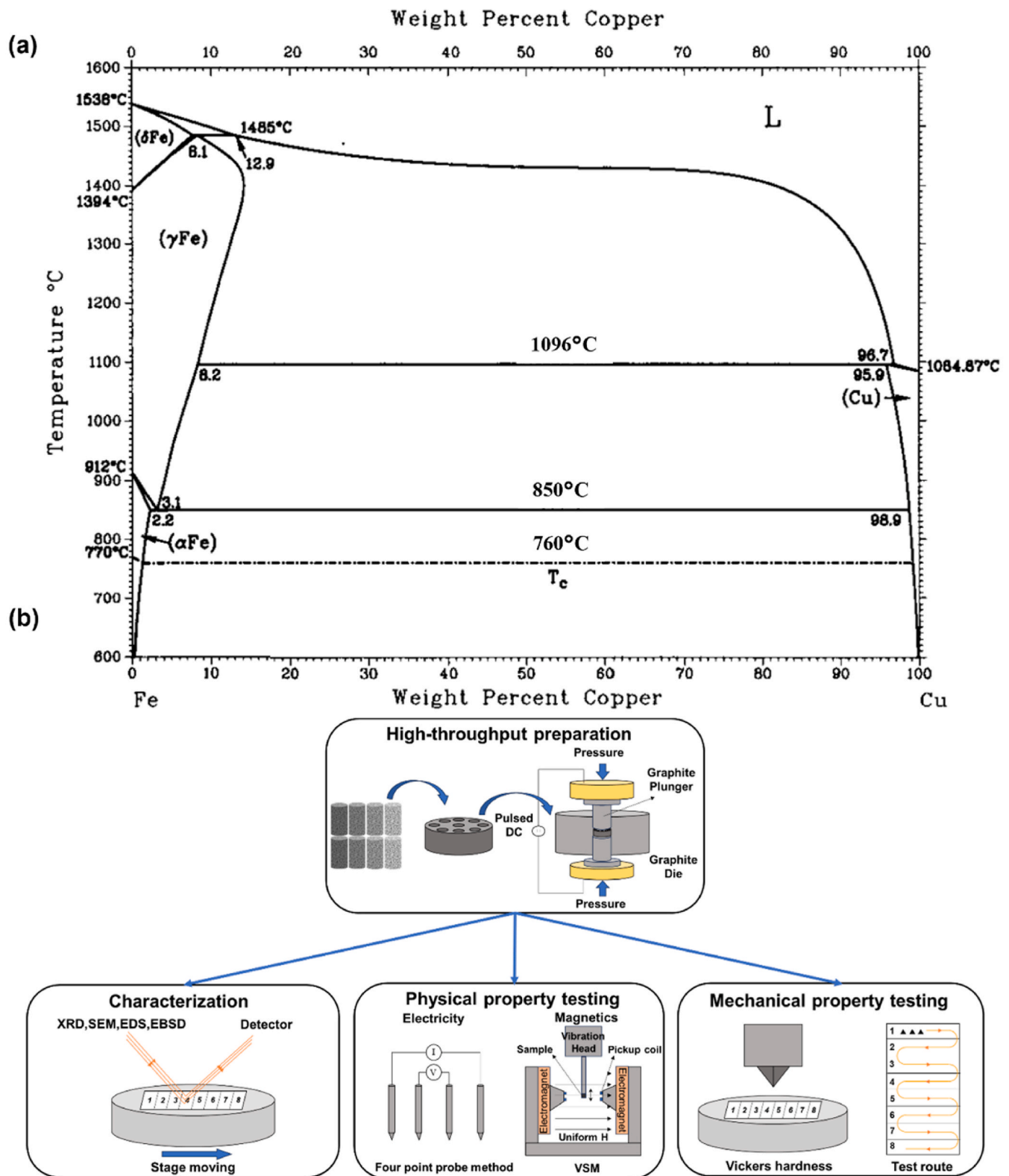
Fig. 1. (a) Phase diagram of Fe–Cu alloy [34] and (b) Schematic diagram of the preparation and accelerated assessment of Fe-xCu alloys.

was present, like that of α-Fe. With a further increase in Cu content, the alloy exhibited a mixture of BCC and face-centered cubic (FCC) phases. An additional 111 diffraction peak corresponding to the FCC phase became more prominent and was clearly present from 8 wt.% Cu onwards. 200 and 220 FCC diffraction peaks were obvious when the content of Cu was increased to 15%.

Fig. 2(c)and (d) are the XRD patterns of as the SPS bulk samples. The diffraction peaks are sharper as compared to the corresponding peaks in Fig. 2(a)–(b), due to the improved crystallinity after the sintering process [35]. Like the powder samples, the BCC peaks of the as SPS samples first appeared in alloys containing 1–3 wt.% Cu. However, the 111 FCC peak became apparent from Fe–4Cu onwards, while the peak for 200
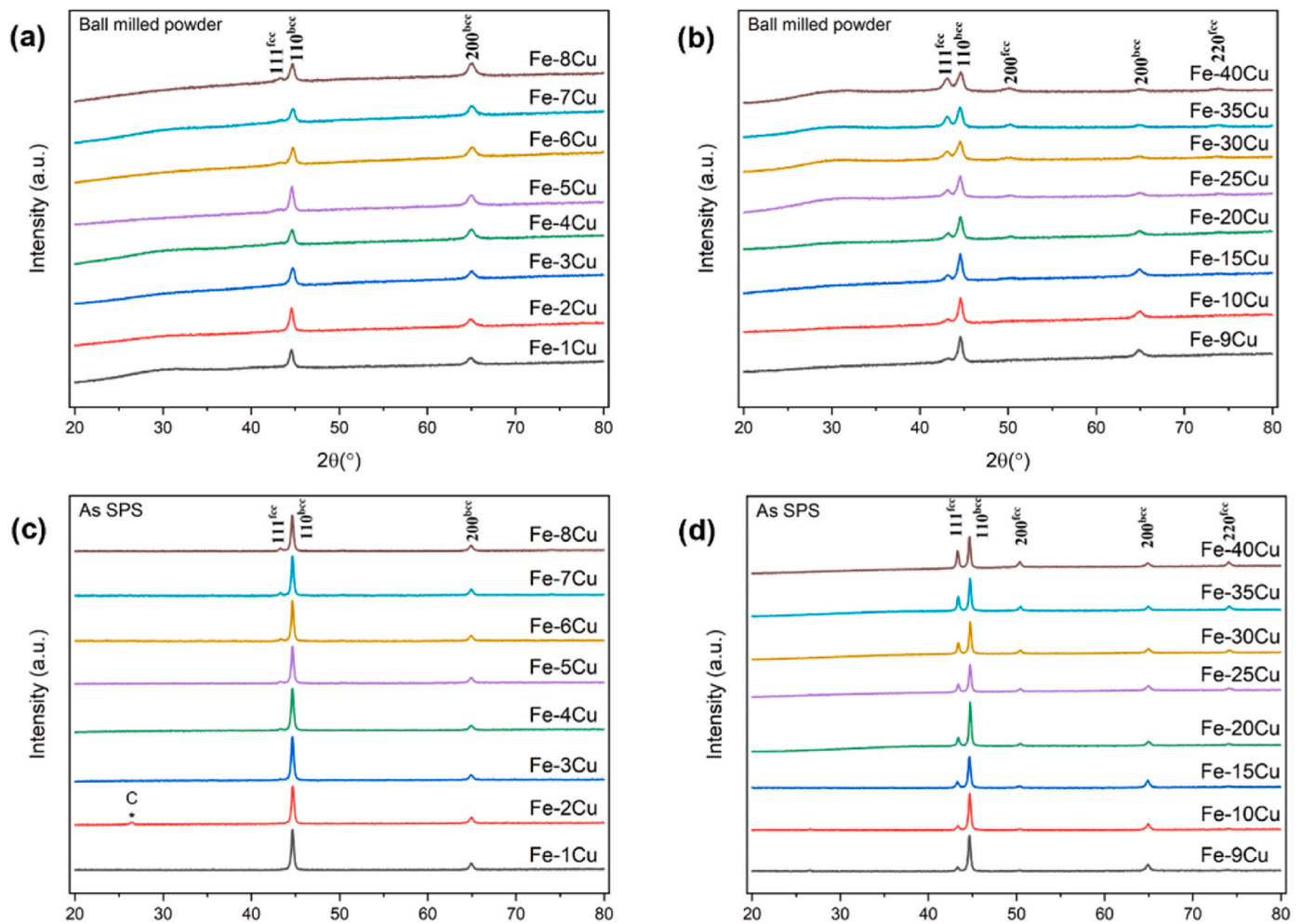
Fig. 2. XRD patterns of (a–b) as ball milled powders, (c–d) as SPS alloys.

FCC was noticeable from Fe-9Cu. After the SPS process, due to the thermal history, some of the defects were removed and stresses were relieved, improving the crystallinity, hence the 111 peak started appearing in lower Cu content samples. The small peak (at 26.6°) in the XRD pattern of Fe–2Cu was attributed to a carbon peak, due to the presence of remnant graphite paper (used in SPS) on the sample surface.

The phase fractions of BCC and FCC phases and the lattice parameters for selected compositions were determined using TOPAS, and shown in Table 1. The crystallite sizes shown were from the volume weighted mean (LVol-IB) calculation in TOPAS.

The phase fraction for these alloys presented in Table 1 differed from the observations of Awadhi et al. [24] and Chien et al. [27]. In their work, binary phases were observed in Fe_xCu_{100-x} ($60 \leq x \leq 75$) compositions. This deviation may be due to the different processing methods, e.g., sputtering [27] or different mechanical alloying

conditions (600 rpm for 10 h) [24] compared to that in our work.

The lattice parameters and crystallite sizes of the BCC and FCC phases are also presented in Table 1. The lattice parameters for the BCC and FCC phase varied from ~2.874 to ~2.878 Å, and from ~3.623 to ~3.629 Å, respectively. The BCC phase exhibited slightly larger lattice parameters than BCC_{Fe} (2.872 Å, from PCPDF card number 04-002-8917) due to the solid solution alloying of Cu into Fe. The lattice parameter for FCC_{Cu} is ~3.604 Å (from PCPDF card number 00-004-0836), while the values obtained for the FCC phase were slightly larger. Thus, the second phase is not a straightforward solid solution alloying of Fe into Cu (where the lattice parameter is expected to be smaller than 3.604 Å). It is possible that this phase formed as a physical reaction between Cu and Fe during the mechanical alloying. The crystallite size range calculated from TOPAS was consistent for BCC and FCC phases, at 30.6–39.7 nm and 25.3–29.9 nm, respectively.

Table 1
Phase fractions and crystal structure information of the as SPS Fe-xCu alloys calculated by TOPAS.

Composition	BCC %	FCC %	Lattice parameter BCC (Å)	Crystallite size BCC (nm) (LVol-IB)	Lattice parameter FCC (Å)	Crystallite size FCC (nm) (LVol-IB)
Fe–1Cu	100	–	2.8753	30.6	–	–
Fe–5Cu	95.2	4.8	2.8755	31.2	3.6252	26.0
Fe–10Cu	89.6	10.4	2.8768	32.6	3.6267	28.0
Fe–15Cu	84.1	15.9	2.8776	29.9	3.6292	25.3
Fe–20Cu	79.4	20.6	2.8776	39.7	3.6292	26.6
Fe–25Cu	75.9	24.1	2.8764	33.5	3.6261	28.0
Fe–30Cu	69.4	30.6	2.8775	35.0	3.6278	27.6
Fe–35Cu	65.2	34.8	2.8759	36.3	3.6255	29.8
Fe–40Cu	58.6	41.4	2.8744	36.4	3.6234	29.9

3.2. Microstructure, phase and texture analysis using backscattered electron microscopy and electron backscatter diffraction

The densities of the as SPS samples measured by Archimedes method were in the range of ~93%–~96% of the theoretical density. Fig. 3 shows the backscattered electron (BSE) micrographs of as SPS Fe-xCu alloys for the various compositions. The vertical direction in the figure is the compression direction of the SPS, the streamlines observed in the microstructure are perpendicular to the pressure direction.

With the Cu content increasing from 1 to 40 wt.%, the content of the white phase in the backscattered electron images increased significantly, and the parallel white banded structure changed to a white reticular structure. Between 1 and 5 wt.% Cu, the microstructure comprises of a grey matrix with discontinuous white banded precipitates, as shown in Fig. 3(a)–(e).

When the copper content increased from 6 to 15 wt.%, the white striped precipitates became connected and separated the grey α-Fe matrix to form a lamellar structure, as illustrated in Fig. 3(f)–(k).

When the copper content was more than 20 wt.%, the layers progressively deformed and interconnect vertically and horizontally to form a mesh-like structure, thereby fully isolating the grey matrix phase, as shown in Fig. 3(l)–(o). From Fig. 3(p), the white precipitate phase volume fraction dominates when the Cu is 40 wt.%.

The band structure was formed due to the nature of the ball milled powders, which were in the form of flat flakes at low Cu content, and evolved to a mixture of small flakes and particles at high Cu content (refer to Fig. S1 in Supporting Information (SI) for more details).

At low Cu content, when the powders were filled in the graphite die for SPS, the flakes would tend to lie on the flat side. Due to the rapid sintering nature of the SPS process, these features would be preserved, appearing as banded structures.

As the powders became smaller flakes and more particle-like, the
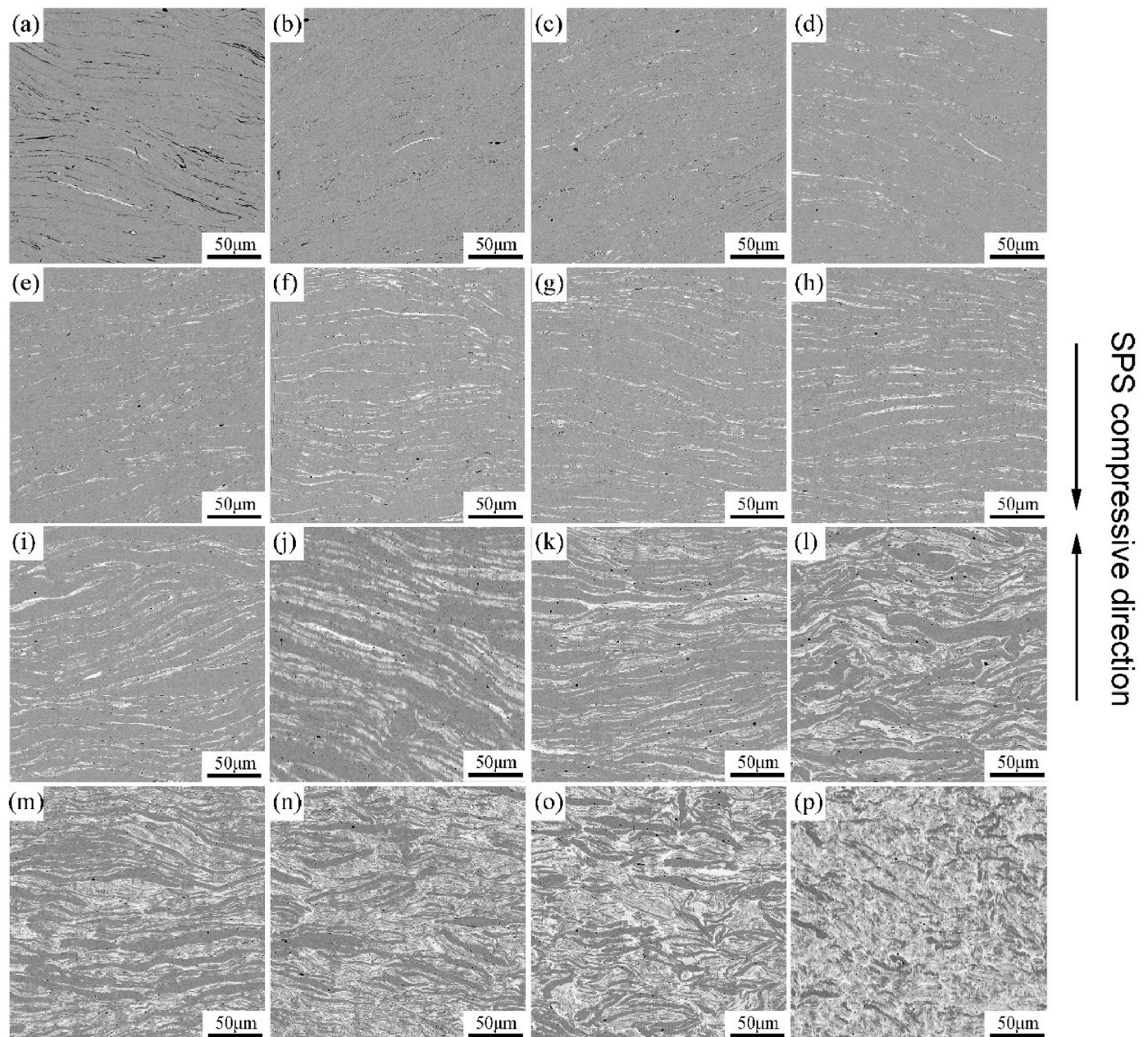
Fig. 3. Backscattered electron micrographs of Fe-xCu alloys (x = 1–40 wt.%). (a)–(p) represent the Cu content of 1, 2, 3, 4, 5, 6, 7, 8, 9, 10, 15, 20, 25, 30, 35 and 40 wt.%, respectively.

band structures evolved into a reticular structure, which can be explained as follows: With the increase of Cu content, the presence of a Cu in Fe would also increase. As the solid solubility of Cu in Fe (and vice versa) is very limited, the Fe-rich matrix would be separated by the Cu-rich layer rather than forming a compound, and the spacing separated by Cu-rich layer would also decrease due to the increase of Cu content.

As the morphology of ball milled powders changed, the adjacent Cu-rich layers and Fe-rich matrix became Cu-rich and Fe-rich regions. Eventually these adjacent Cu-rich regions became close enough to be connected to form a network structure.

EDX analysis was carried out on the phases with differing contrast in the microstructure and the results are shown in Table S1 in the SI. The Fe-xCu alloy consisted mainly of a grey matrix phase and white precipitates. The grey matrix phase was dominated by Fe, whose content ranged from 98.23 to 99.74%. The Fe content showed a decreasing trend with increasing Cu content, but the total range of Fe content fluctuation was within 1.5%. Although the solid solubility of Cu in BCC Fe is low, at 0.35% below 600 °C, the ball milling process had increased the solubility limit slightly. The content of Cu in the white phase was high, ranging from 54.5 to 87.7%, indicating that the white phase was a Cu-rich phase. The EDX information confirmed the solid solution alloying of Fe and Cu in the matrix and the presence of the second phase. A small amount of a black phase or omitted porosity appeared as interlayer bands or was distributed randomly within the grey matrix, and contained the elements Fe, C and O.

The software Image-Pro Plus was used for the calculation of the volume fraction of this Cu-rich second phase (white phase), and the results are shown in Table 2. The volume fraction of the white phase in Fe-xCu alloys increased from 0.13 to 57.54%.

Phase maps are presented in Fig. 4 and the corresponding phase ratios of Fe-BCC to Fe-FCC are presented in Table 2. Overall, the Fe-BCC phase was the majority phase with an increase in Fe-FCC content with Cu addition, as observed in the XRD patterns of Fig. 2. Comparing the phase ratio to the volume fraction of the white phase in Table 2, this increase in the Fe-FCC phase had a direct correlation to Cu content at higher Cu loading. At lower loadings, however, the deviation from the ratio was larger. This could be attributed to the fine nanosized grains which were highly stressed by the ball milling process and were difficult to index *via* EBSD, hence the signals were not picked up as the Fe-BCC phase. The grain size distribution of as SPS samples calculated from the area weighted mean average from EBSD is also shown in Table 2.

The out-of-plane crystallographic texture maps obtained by EBSD are presented in Fig. 5 and were used in addition to inverse pole figures (Figs. S2 and S3 in the SI) to characterize Fe-xCu alloys for their grain size and preferred crystallographic orientation.

Overall, the Fe-BCC grains in the Fe-xCu alloys exhibited a low strength <001> texture with maximum multiple of uniform density (MUD) values between 1.26 and 2.94 (Figs. S2 and S3). This texture preference is common in ferrous cubic alloys as it is the fast grain growth direction and follows the direction of heat flow, sintering current and pressure [36].

This texture weakened with increasing Cu content due to it stabilizing the Fe-FCC phase and refinement of the grains. Comparatively, Fe-FCC grains showed a weak <111> texture preference characteristic of Σ3 grain boundaries, the texture direction with the minimum energy [37].

Overall, both phases presented weak crystallographic textures, exhibited in a range of cubic alloys processed by mechanical alloyed and pre-alloyed powders [38–43].

The grain size decreased significantly with an increase of Cu content, as represented in the statistical results shown in Table 2. Overall, the average grain sizes of Fe–Cu alloys obtained from mechanical alloying and spark plasma sintering were small and distributed between 4.36 and 9.47 μm. As mechanical alloying involved the crushing and alloying of fine powder, followed by spark plasma sintering under conditions of pressure and rapid heating and cooling, the grain sizes obtained were small. The corresponding particle sizes and crystallite sizes of selected compositions of the ball milled powders were obtained from secondary electron imaging and volume weighted mean (LVol-IB) calculations in TOPAS, from its XRD patterns, respectively. These are shown in Fig. S1 and Table S2 in the SI.

When Cu was added in low concentrations, the spacing between the layers in the matrix increases, with each layer width being the grain width. Additionally, there were fine grains dispersed among the large grains in each layer. As the Cu content increased, the spacing between the layers decreased, along with the size of the larger grains, while the volume fraction of the smaller grains increased. Upon comparison of the EDX and EBSD maps, it was evident that the region in which the fine grains were situated was a white Cu-rich phase, whereas the region containing the large grains was a Fe-rich matrix phase, as seen in Figs. 3–5.

As the Cu content increased, Cu-rich particles aggregated in the interlayer, forming small grains. Simultaneously, the interlayer also broke up the Fe-rich matrix, while reducing the grain size. When the Cu addition exceeded 20 wt%, the interlayer distribution along the compression direction was less obvious. The orientation was disrupted by an increase in the Cu-rich phase content, the arrangement of grains changed from a fixed orientation along the layer to a random distribution. The reduction in average grain size presented in Table 2 was attributed to two factors. Firstly, the Fe-rich matrix was partitioned because of the increased Cu-rich phase content. Secondly, an increase in small grains of the Cu-rich phase led to a decrease in the average grain

Table 2
Data related to microstructure of as SPS Fe-xCu alloys.

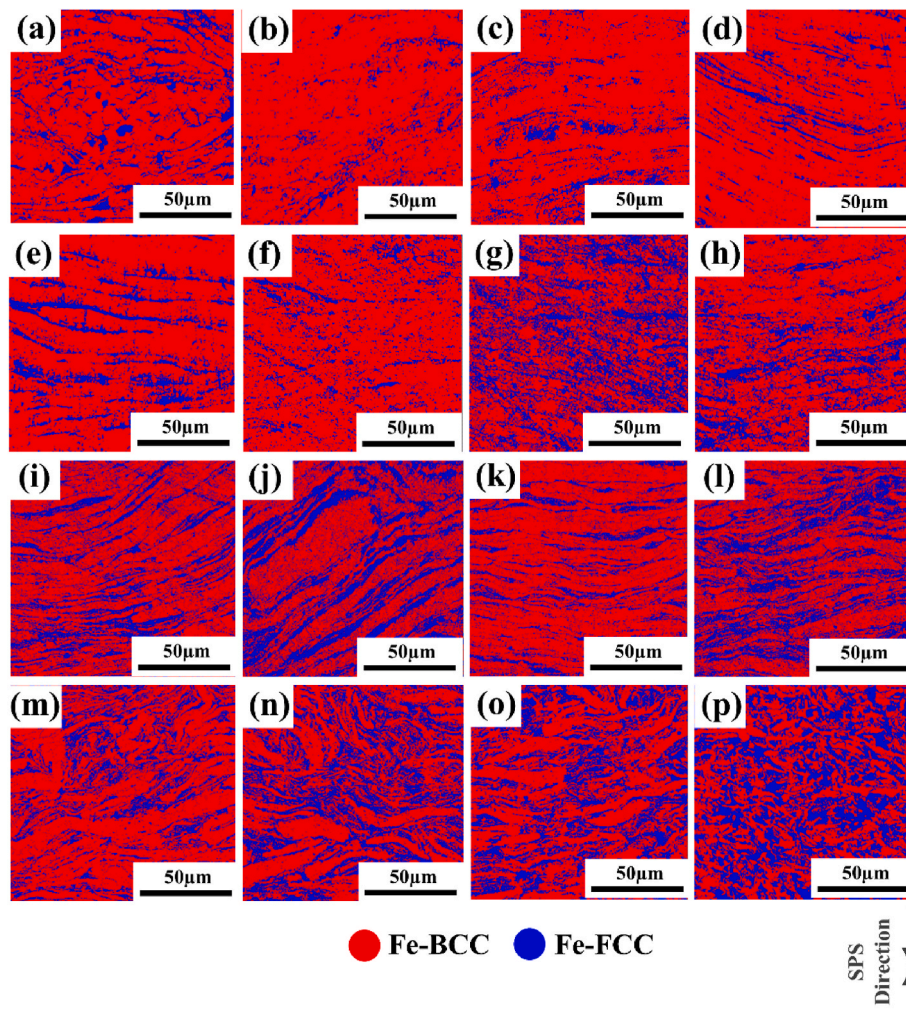| No.	Composition (wt. %)	Volume fraction of white phase ($V_{white\ phase}$) (%)	Fe-BCC:Fe-FCC (from EBSD) (%)	Grain size of BCC phase (μm) (from EBSD)	Standard deviation (μm)	Grain size of FCC phase (μm) (from EBSD)	Standard deviation (μm)
1	Fe–1Cu	0.13	83.4:16.6	6.83	2.30	–	–
2	Fe–2Cu	0.36	90.4:9.6	9.47	3.47	–	–
3	Fe–3Cu	0.74	89.6:10.4	9.42	3.28	–	–
4	Fe–4Cu	2.03	89.5:10.5	7.38	2.65	0.39	0.11
5	Fe–5Cu	3.09	80.0:20.0	5.81	2.15	0.37	0.11
6	Fe–6Cu	4.90	85.8:14.2	6.89	2.50	0.48	0.14
7	Fe–7Cu	6.84	63.6:36.4	5.39	1.81	0.46	0.13
8	Fe–8Cu	8.81	73.6:26.4	6.21	2.18	0.58	0.16
9	Fe–9Cu	9.91	72.9:27.1	6.16	2.23	0.50	0.13
10	Fe–10Cu	18.52	71.0:29.0	4.44	1.38	0.45	0.12
11	Fe–15Cu	20.92	78.2:27.2	5.69	2.04	0.73	0.13
12	Fe–20Cu	27.96	65.5:34.5	5.20	1.78	0.70	0.10
13	Fe–25Cu	28.54	75.6:24.4	6.37	2.08	0.60	0.20
14	Fe–30Cu	38.09	62.8:37.2	5.10	1.60	0.60	0.10
15	Fe–35Cu	41.22	66.7:33.3	5.70	1.90	0.90	0.20
16	Fe–40Cu	57.54	56.4:43.6	4.36	1.52	1.23	0.24

Fig. 4. Phase maps of Fe-xCu alloys, (a)–(p) represent the Cu content of 1, 2, 3, 4, 5, 6, 7, 8, 9, 10, 15, 20, 25, 30, 35 and 40 wt.%, respectively.

size.

3.3. Magnetic properties

Fig. 6(a) and (b) show the field dependence of magnetization at room temperature. From Fig. 6(c), the saturation magnetization (M_s) of as SPS samples are in the range of 211.3–118 emu/g, while the coercivity (H_c), are in the range of 14.6–45.7 Oe. M_s generally decreased and the H_c increased as the content of Cu increases in Fe-xCu alloys. M_s is a function of the magnetic moment [44]. Cu is a diamagnetic element, and an increase in its content will reduce the net magnetic moment in the alloy, resulting in a decrease in its M_s. For H_c, the variation may be related to microstructure related parameters, e.g., second phase precipitates and boundaries, defects, variation in grain size, etc. Although grain size changes were limited to a small range, a significant increase in the small Cu-rich second phase content increased the phase boundaries present in the alloy, which could impede the magnetic domains as they move and ultimately increased the H_c of the alloy (refer to Fig. 7). Due to the sensitivity to multiple factors, it is common to not have a monotonic trend in H_c values with composition [45]. We tried to understand the effect of band structures on H_c in the samples by applying magnetic fields along and across the band structure, but there was no significant difference in the H_c values.

The values of the Curie temperature (T_c) measured using a magnet assisted TGA method [14,32] are shown in Fig. 6(d). T_c ranged from ~753 to ~757 °C, close to the value of 760 °C in the phase diagram shown in Fig. 1(a). There was an additional transition at lower temperatures of ~720 and ~727 °C observed for Fe–30Cu and Fe–40Cu, respectively, indicating that at these compositions, the second phase played a role in the magnetic transitions.

Based on the microstructural results presented in Fig. 3 and Table 2, the addition of Cu increased the fraction of the white Cu-rich second phase in Fe-xCu alloys from 0.13 to 57.54%. Meanwhile, changes in grain size showed an overall decreasing trend with slight fluctuations.

Fig. 7 shows the plot between the $1/D_g$ (D_g is the grain size) and H_c of Fe-xCu alloys. The oval shape covering the points shows a general trend of decreasing grain size and increasing H_c. This inverse relationship between grain size (in the micron size range) and coercivity is similar to that presented in the Herzer plot [46].

For example, the grain sizes of Fe–4Cu, Fe–5Cu and Fe–6Cu first decreased and then increased, while the values of H_c showed a tendency to increase and then decrease. There is a correlation between H_c and the grain size, as shown in Equation (2):

When the size of grain is larger than the size of the magnetic domain [46],

$$H_c = 3 \frac{(k T_c K_1/a)^{1/2}}{J_s} \times \frac{1}{D_g} \tag{2}$$

where H_c is the coercivity, K_1 is the anisotropy constant, J_s is the saturation polarization, k is the Boltzmann constant, a is the lattice parameter, T_c is the Curie point, D_g is the grain size.
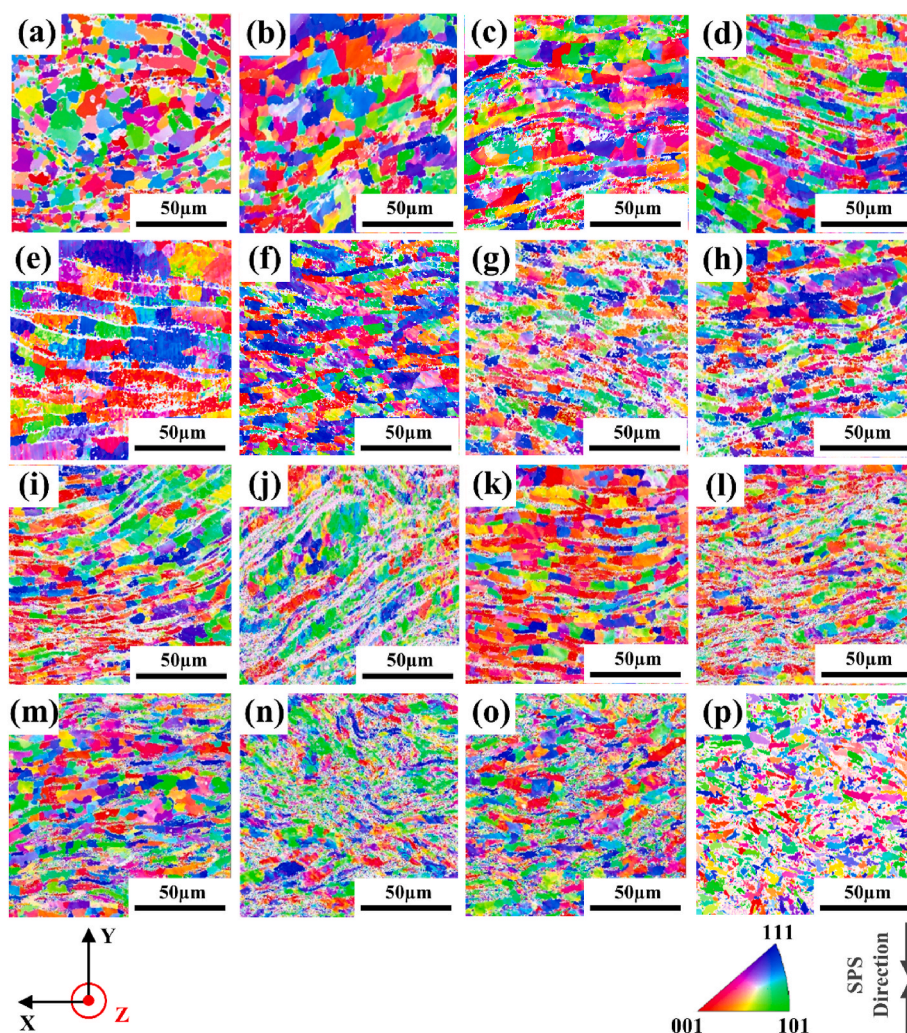
Fig. 5. Crystallographic texture maps of Fe-xCu alloys taken out-of-plane (Z direction), (a)–(p) represent the Cu content of 1, 2, 3, 4, 5, 6, 7, 8, 9, 10, 15, 20, 25, 30, 35 and 40 wt.%, respectively.

In this study, the grain sizes obtained by mechanical alloying and SPS were distributed between 4.36 μm and 9.47 μm, which is much larger than the domain width of a typical soft magnetic alloy. The smaller grain sizes of the second phase were in the range of ~0.4–1.2 μm, near the size of the magnetic domains. Typical domain widths range from a few nanometers to several hundred nanometers in soft magnetic alloys. Shi et al. [47] investigated FeCoNiGd alloy and found magnetic domain widths between 0.42 μm and 0.69 μm, and Zhou et al. [48] found that the magnetic domain width of a Fe-3wt.%Si alloy was between 0.8 and 1.3 μm. Considering the trend observed, the smaller grain sizes of the second phase may not have much influence on H_c, except for Fe–40Cu. Other than Fe–40Cu, H_c was inversely proportional to the grain size and decreased as the grain size increased.

3.4. Electrical properties

Fig. 8 shows the electrical resistivity as a function of Cu content. The values for as SPS samples ranged from 27.3 to 40.9 μΩ·cm. The resistivity value decreased slightly from 1 wt.% Cu to 2 wt.% Cu, then generally increased with Cu content until 4 wt.%, before decreasing in value to 25 wt% Cu and finally slowly increasing until 40 wt.% Cu. For reference, the electrical resistivity of Fe and Cu are 10 μΩ·cm and 1.7 μΩ·cm, respectively [49].

The resistivity values of the alloys were about 3–4 times more than that of Fe, indicating that solid solution behavior led to an overall synergistic effect (with the effect most obvious in low Cu content); the presence of two phases also played a role. The layered microstructures present could increase the area of the scattering boundaries. With increasing Cu content, lower resistivity values were obtained, and the microstructure was observed to change from a parallel white banded structure to a white reticular structure. In addition, due to the nature of processing *via* mechanical alloying, there would be more grain boundary area from the compacted powders as compared to a bulk alloy, which increased the resistivity.

For a low concentration solid solution alloy, the electrical resistance ρ is described by Matthiessen's rule in Equation (3) [50]:

$$\rho = \rho_t + \rho_b + \rho_I + \rho_d \tag{3}$$

where ρ_t, ρ_b, ρ_I, and ρ_d represent the thermal, grain boundary, impurity, and dislocation contributions, respectively. As the Cu content increased, the grain size decreased and the fraction of second phase increased, leading to a greater number of grain and phase boundaries. Consequently, the ρ_b and ρ_I factors led to increased electron scattering, which led to larger resistivity of the alloy. Some deviations from the trend (e.g., in samples with 2%, 7% and 40% Cu) may be due to the various factors mentioned in Equation (3) being sensitive to the differences in the condition of the samples. Electrical resistivity measurements were measured in the same direction for all samples, i.e., parallel to their length, for consistency. However, there is a possibility of anisotropy in
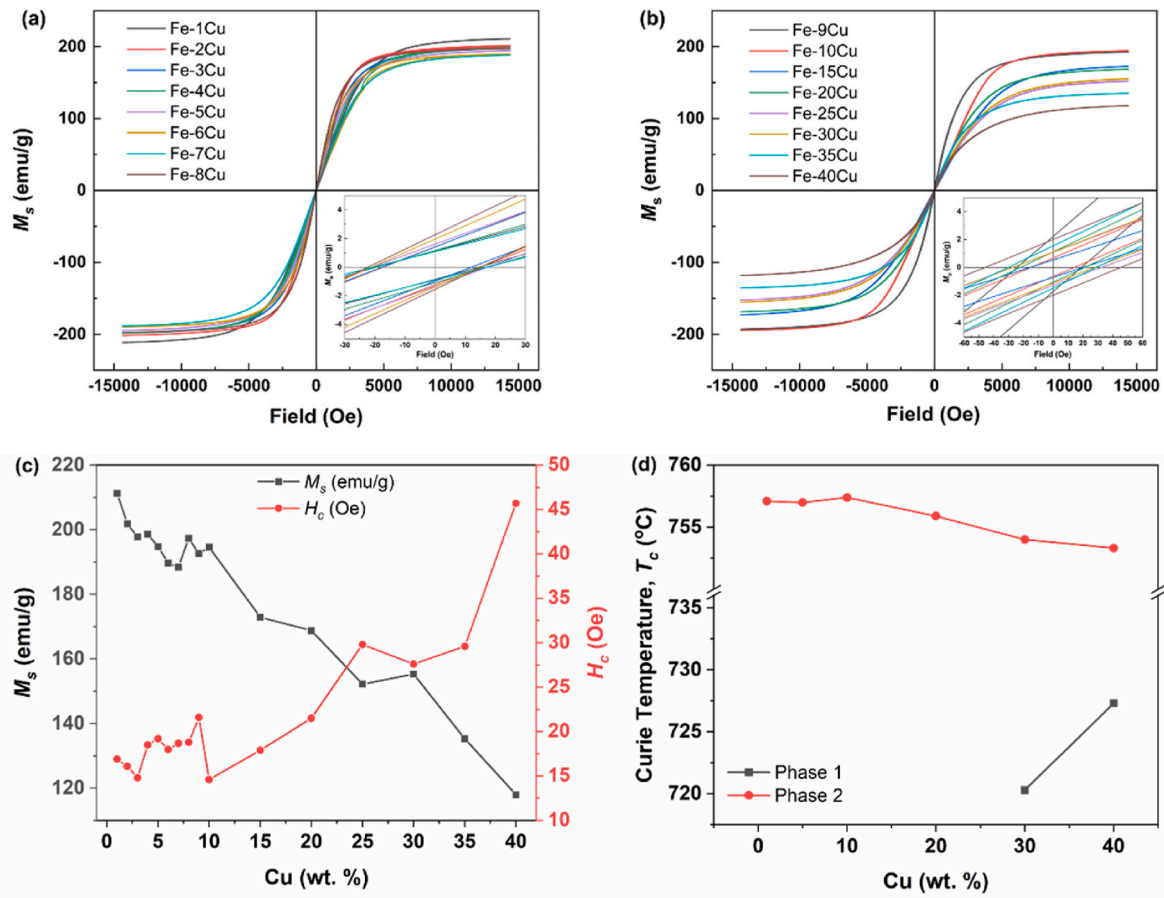
Fig. 6. Magnetic properties of as SPS Fe-xCu alloys. (a,b) Field dependence of magnetization at room temperature, (c) Saturation magnetization (M_s, left axis, black squares) and coercivity, (H_c, right axis, red spheres) and (d) Curie temperature, T_c, as a function of Cu content. (For interpretation of the references to colour in this figure legend, the reader is referred to the Web version of this article.)
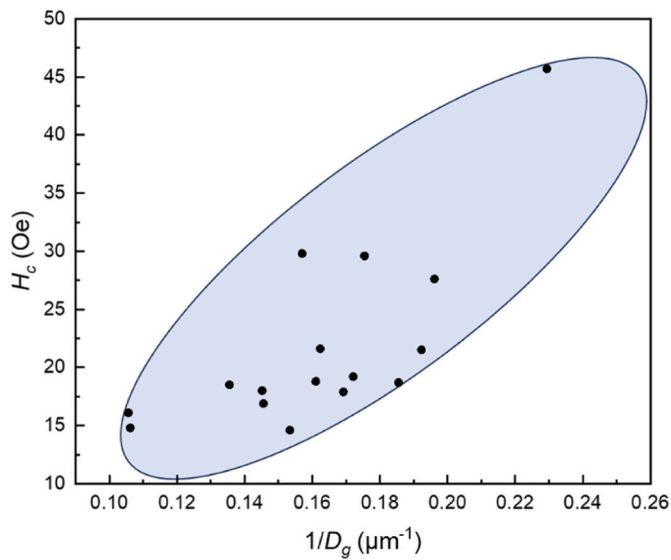

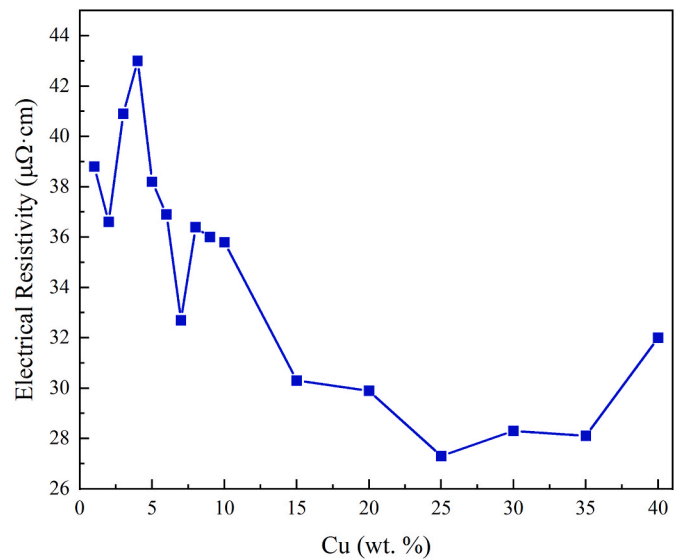**Fig. 7.** Change in H_c with $1/D_g$ for Fe-xCu alloys.

Fig. 8. Electrical resistivity of Fe-xCu alloys as a function of Cu content.

resistivity due to the presence of a banded microstructure. Due to the limited dimension of the samples, resistivity measurements could not be done in the perpendicular direction to verify it.

3.5. Mechanical properties

Fig. 9 shows the changing trend of hardness values of Fe-xCu alloys with an increase of Cu content. When the addition of Cu was low (1–10 wt.%), its hardness fluctuated in a small range, but the overall trend was
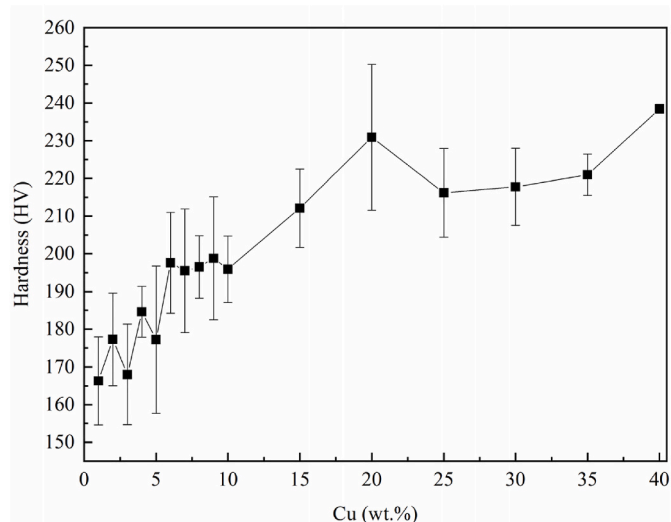
Fig. 9. Vickers hardness of Fe-xCu alloys.

an increase of hardness. For the addition of 15–20 wt.% Cu, the hardness value significantly increased, and with an increase of Cu to 40 wt.%, the hardness value decreased slightly, and then continued to increase.

Electromagnetic-mechanical devices for energy conversion require materials with efficient electrical and magnetic properties. Being mechanical devices, they also need to have certain processability and good mechanical properties. Hardness is one of the quickest ways to reflect a material's ability to resist deformation and is used as a proxy to indicate its mechanical properties. Our experimental findings above demonstrated an increase in the hardness of Fe-xCu alloys as the Cu content increased. This alteration in hardness could potentially be influenced by various factors:

I. According to the relationship between grain size and Vickers hardness, it can be seen in Fig. 10 that with an increase in Cu content, the overall trend of grain size is decreasing, while the hardness of the alloy has an overall upward trend. The Hall-Petch relationship predicts an inverse relationship between the grain size and the resistance to dislocation motion. The smaller the size of the grain, the
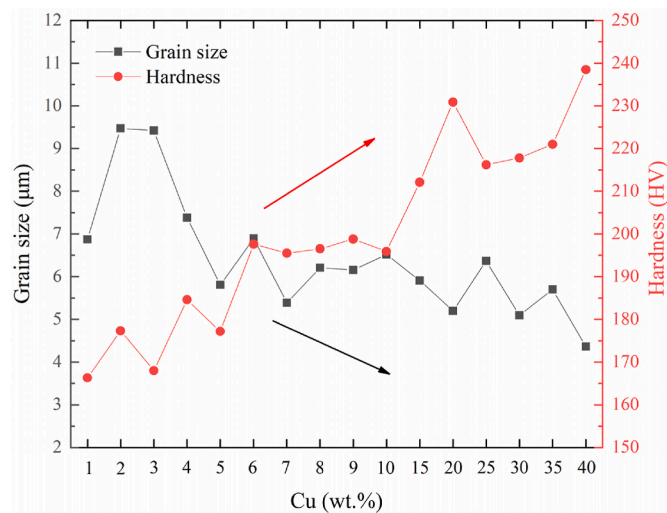

Fig. 10. Relationship between grain size (left axis, black squares) and hardness (right axis, red spheres) of Fe-xCu alloys. (For interpretation of the references to colour in this figure legend, the reader is referred to the Web version of this article.)

stronger the obstruction to the dislocation motion, leading to a higher hardness.

II. From a constituent phase standpoint, the alloy underwent a transformation from a BCC phase to binary BCC + FCC phases with increased content of Cu. The introduction of Cu into the alloy matrix resulted in the formation of a Cu-rich FCC precipitate, which led to an enhancement in the hardness of the alloy. Although the solubility of Cu in Fe is low, not exceeding 0.35% at room temperature, mechanical alloying can change this solubility limit, since it a non-equilibrium process. As the amount of Cu increased, the content of Cu-containing precipitates within the Fe–Cu alloy matrix also increased, which impeded dislocation motion during deformation and consequently increased the alloy's hardness.

3.6. Accelerated screening

The microstructure and a range of material properties of Fe-xCu alloys were investigated using accelerated methodology, and the effect of Cu content on the microstructure, electrical properties, magnetic properties and mechanical properties of Fe–xCu alloys were investigated. Fig. 11(a) shows the plot for the 16 compositions for 4 properties – M_s, $1/H_c$, electrical resistivity and microhardness (more information is provided in Table S3 in the SI). As lower H_c values are more ideal, $1/H_c$ was used so that selection of a sample with attractive H_c would be the one with a larger $1/H_c$ value, similar to the metrics for other material properties.

From Fig. 11(a), based on the current processing variables, 3 compositions, Fe–3Cu, Fe–4Cu and Fe–10Cu, were identified as potential compositions for future development. Fe–4Cu had the highest electrical resistivity (blue arrow), while Fe–10Cu had the lowest coercivity (red arrow), amongst all samples. Fe–3Cu did not possess the highest values for all the measured material properties, but it had attractive values for the other three properties (circled in purple), with microhardness being slightly low. The range of these material properties were between 195 and 199 emu/g, 14.6–18.5 Oe, 36–43 μΩ·cm and 168–196 HV, comparable to currently used soft magnetic materials [51]. With a high T_c of ~757°C, they are potentially attractive for energy applications.

Fig. 11(b) shows the M_s vs Vickers hardness for these 3 alloys with representative soft magnetic alloys, e.g., iron, permalloy, permendur, $Fe_{52}Ni_{48}$, low Si content grain oriented (GO) or non-oriented (NO) Fe–Si and nanocrystalline alloys (FINEMET). The 3 Fe-xCu alloys possessed properties close to commonly used low Si content alloys, and better than Fe–Ni based alloys. It also has the added advantage of being a binary alloy system and cheaper than cobalt containing alloys. This will be beneficial for reducing total cost of production.

Fig. 12 shows a heat map of the Pearson's correlation coefficients with composition and other parameters prepared from the accelerated methodology data of the Fe-xCu alloys. The maximum positive correlation coefficient of 0.99 was obtained for the Cu content and the volume fraction of the Cu-rich white phase. A positive correlation indicates that when the value of one parameter increases, there is a tendency for the other to increase as well. The maximum negative correlation coefficient of −0.98 was obtained from the Cu content and saturation magnetization.

The above results show that H_c and hardness were positively correlated with Cu additions, while M_s and resistivity were inversely correlated, which calls for the need to comprehensively consider the trends of multiple properties in the selection of magnetic alloys, such as ensuring higher magnetic properties, i.e., high M_s and low H_c, and improving the alloy hardness and resistivity as much as possible. Especially for M_s and H_c with strong correlation, relatively low Cu element addition is conducive to maintaining high magnetic properties without much deterioration of other properties.

These results indicate that our approach of using accelerated methodologies can rapidly establish the correlation between composition and multiple properties, providing optimal conditions for screening
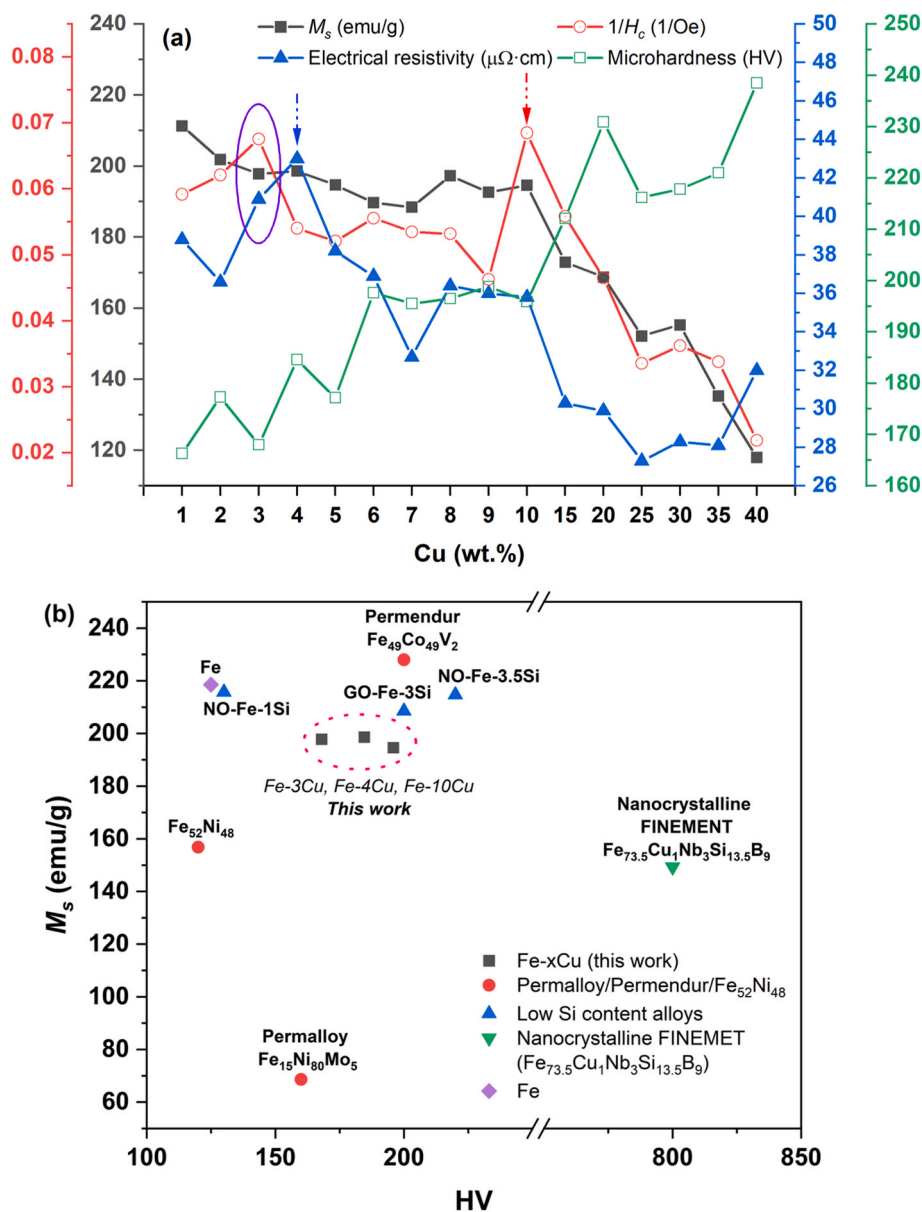
Fig. 11. Plot of (a) various material properties vs Fe-xCu alloys and (b) M_s vs HV of selected Fe-xCu alloys and representative soft magnetic materials [51].

components and determining novel potential attractive compositions. This accelerated approach can also expand the materials database. A summary of the results obtained for all 16 compositions is included in Table S4 in the SI. This in turn can provide support to the future development of this family of alloys *via* machine learning approaches, and meet the growing demand for these properties in applications such as electric motors and electronic products.

4. Conclusions

In this study, Fe-xCu alloys were synthesized using an accelerated method of mechanical alloying and HT spark plasma sintering. The microstructure and multiple properties of the alloys were characterized and analyzed.

The findings suggest the following conclusions:

1. As the Cu increases from 0 to 40 wt.%, the proportion of Cu-rich phase increased from 0.13% to 57.54%, and the constituent phases changed from BCC to FCC + BCC. Additionally, the grain size varied between ~4.4 μm and ~9.5 μm for the BCC phase and ~0.4 μm–1.23 μm for the FCC phase.

2. The increase of Cu content led to a decline in the M_s from 211.3 emu/g to 118 emu/g. Conversely, the hardness value increased from 166.3 HV to 238.5 HV, and the H_c changed from 14.6 Oe to 45.7 Oe, while the resistivity changed from 27.3 μΩ·cm to 43.0 μΩ·cm.

3. The increased content of the precipitated phase enriched with the diamagnetic Cu led to a decrease in M_s and grain size, as well as an increase in H_c and hardness.

4. Compositional screening using accelerated methodology experiments can quickly establish the relationship between alloy microstructure and overall performance.

5. Based on the processing parameters, three compositions were identified in this work – Fe–3Cu, Fe–4Cu and Fe–10Cu – that exhibited a balanced set of properties, high electrical resistivity and low coercivity respectively. With comparable M_s vs HV to commonly used soft magnetic materials, they are potentially attractive for energy applications, with the added benefit of lower cost.

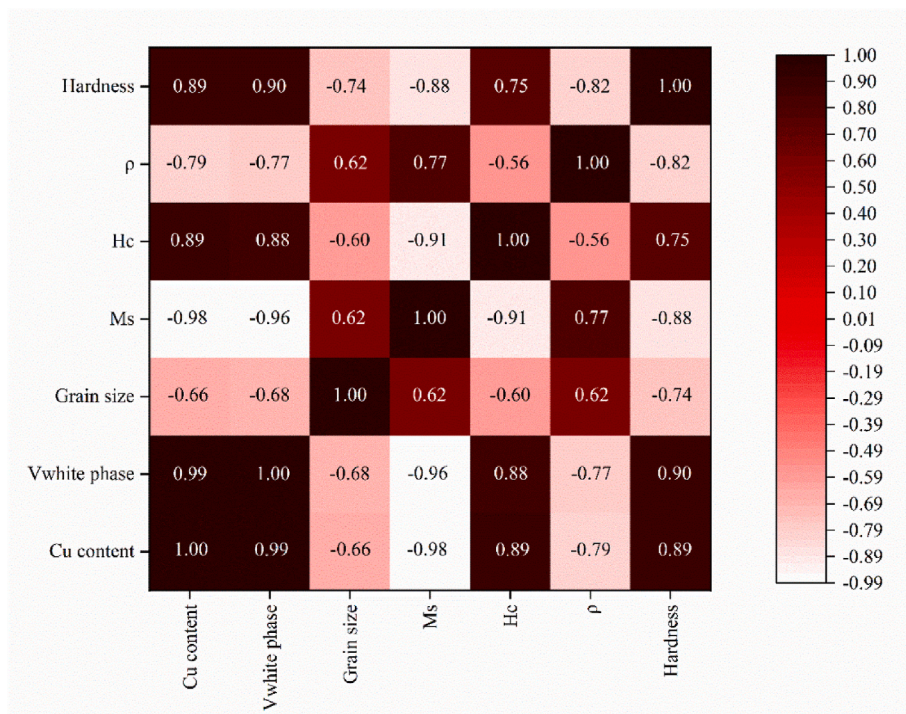Thus, the hypothesis of the work has been validated – the resistivity

Fig. 12. Heat map for the accelerated methodology data of Fe-xCu alloys.

and hardness did increase significantly compared to elemental Fe with increased Cu content. The results presented in this work highlighted the diverse aspects of this material system that can be further investigated to optimize the material properties – the microstructure evolution and the directional effects of the microstructure on electrical resistivity and coercivity. With further investigation and understanding of the ball milled Fe–Cu alloys, better materials can be developed for energy applications.

CRediT authorship contribution statement

X. Xu: Writing – review & editing, Writing – original draft, Visualization, Validation, Methodology, Investigation, Formal analysis. **Li Ping Tan:** Writing – review & editing, Writing – original draft, Validation, Methodology, Investigation, Formal analysis. **Karl P. Davidson:** Writing – review & editing, Visualization, Validation, Methodology, Investigation. **Shakti P. Padhy:** Writing – review & editing, Validation, Methodology. **V. Chaudhary:** Writing – review & editing, Investigation, Supervision, Methodology, Conceptualization. **R.V. Ramanujan:** Writing – review & editing, Supervision, Resources, Funding acquisition, Conceptualization.

Declaration of competing interest

The authors declare that they have no known competing financial interests or personal relationships that could have appeared to influence the work reported in this paper.

Acknowledgement

Appendix A. Supplementary data

Supplementary data to this article can be found online at https://doi.org/10.1016/j.jmrt.2024.08.158.

References

[1] Silveyra JM, Ferrara E, Huber DL, Monson TC. Soft magnetic materials for a sustainable and electrified world. Science 2018;362:1–9. https://doi.org/10.1126/science.aao0195.

[2] Shokrollahi H, Janghorban K. Soft magnetic composite materials (SMCs). J Mater Process Technol 2007;189:1–12. https://doi.org/10.1016/j.jmatprotec.2007.02.034.

[3] Han L, Maccari F, Souza Filho IR, Peter NJ, Wei Y, Gault B, Gutfleisch O, Li Z, Raabe D. A mechanically strong and ductile soft magnet with extremely low coercivity. Nature 2022;608:310–6. https://doi.org/10.1016/10.1038/s41586-022-04935-3.

[4] Agrawal A, Choudhary A. Perspective: materials informatics and big data: realization of the "fourth paradigm" of science in materials science. Apl Mater 2016;4:53208. https://doi.org/10.1063/1.4946894.

[5] Chaudhary V, Chaudhary R, Banerjee R, Ramanujan RV. Accelerated and conventional development of magnetic high entropy alloys. Mater Today 2021;49:231–52. https://doi.org/10.1016/j.mattod.2021.03.018.

[6] Dunlap RA, Sibley GL, Sy FN, Hatchard TD. Combinatorial material science studies of Fe-rich Fe–Al and Fe–Si thin films. J Alloys Compd 2009;470:27–34. https://doi.org/10.1016/j.jallcom.2008.02.066.

[7] Yi Wang W, Li J, Liu W, Liu Z. Integrated computational materials engineering for advanced materials: a brief review. Comput Mater Sci 2019;158:42–8. https://doi.org/10.1016/j.commatsci.2018.11.001.

[8] de Pablo JJ, Jackson NE, Webb MA, Chen L, Moore JE, Morgan D, Jacobs R, Pollock T, Schlom DG, Toberer ES, Analytis J, Dabo I, Delongchamp DM, Fiete GA, Grason GM, Hautier G, Mo Y, Rajan K, Reed EJ, Rodriguez E, Stevanovic V, Suntivich J, Thornton K, Zhao J. New frontiers for the materials genome initiative. npj Comput Mater 2019;5:41. https://doi.org/10.1038/s41524-019-0173-4.

[9] Vecchio KS, Dippo OF, Kaufmann KR, Liu X. High-throughput rapid experimental alloy development (HT-READ). Acta Mater 2021;221:117352. https://doi.org/10.1016/j.actamat.2021.117352.

[10] Santodonato LJ, Liaw PK, Unocic RR, Bei H, Morris JR. Predictive multiphase evolution in Al-containing high-entropy alloys. Nat Commun 2018;9:4520. https://doi.org/10.1038/s41467-018-06757-2.

[11] Yang S, Lu J, Xing F, Zhang L, Zhong Y. Revisit the VEC rule in high entropy alloys (HEAs) with high-throughput CALPHAD approach and its applications for material design-A case study with Al–Co–Cr–Fe–Ni system. Acta Mater 2020;192:11–9. https://doi.org/10.1016/j.actamat.2020.03.039.

[12] Padhy SP, Tan LP, Varma VB, Chaudhary V, Tsakadze Z, Ramanujan RV. Accelerated multi-property screening of Fe–Co–Ni alloy libraries by hyper-heuristic combinatorial flow synthesis and high-throughput spark plasma sintering. J Mater Res Technol 2023;27:2976–88. https://doi.org/10.1016/j.jmrt.2023.10.124.

[13] Tan LP, Chaudhary V, Tsakadze Z, Ramanujan RV. Rapid multiple property determination from bulk materials libraries prepared from chemically synthesized powders. Sci Rep 2022;12:9504. https://doi.org/10.1038/s41598-022-13691-3.

[14] Chaudhary V, Tan LP, Sharma VK, Ramanujan RV. Accelerated study of magnetic Fe-Co-Ni alloys through compositionally graded spark plasma sintered samples. J Alloys Compd 2021;869:159318. https://doi.org/10.1016/j.jallcom.2021.159318.

[15] Teh WH, Chaudhary V, Chen S, Lim SH, Wei F, Lee JY, Wang P, Padhy SP, Tan CC, Ramanujan RV. High throughput multi-property evaluation of additively manufactured Co-Fe-Ni materials libraries. Addit Manuf 2022;58:102983. https://doi.org/10.1016/j.addma.2022.102983.

[16] Padhy SP, Tsakadze Z, Chaudhary V, Lim GJ, Tan X, Lew WS, Ramanujan RV. Rapid multi-property assessment of compositionally modulated Fe-Co-Ni thin film material libraries. Results in Materials 2022;14:100283. https://doi.org/10.1016/j.rinma.2022.100283.

[17] Han L, Rao Z, Souza Filho IR, Maccari F, Wei Y, Wu G, Ahmadian A, Zhou X, Gutfleisch O, Ponge D, Raabe D, Li Z. Ultrastrong and ductile soft magnetic high-entropy alloys via coherent ordered nanoprecipitates. Adv Mater 2021;33: 2102139. https://doi.org/10.1002/adma.202102139.

[18] Ma Y, Wang Q, Zhou X, Hao J, Gault B, Zhang Q, Dong C, Nieh TG. A novel soft-magnetic B2-based multiprincipal-element alloy with a uniform distribution of coherent body-centered-cubic nanoprecipitates. Adv Mater 2021;33:2006723. https://doi.org/10.1002/adma.202006723.

[19] Li Z, Zhang Z, Liu X, Li H, Zhang E, Bai G, Xu H, Liu X, Zhang X. Strength, plasticity and coercivity tradeoff in soft magnetic high-entropy alloys by multiple coherent interfaces. Acta Mater 2023;254:118970. https://doi.org/10.1016/j.actamat.2023.118970.

[20] Wang Z, Yuan J, Wang Q, Li Z, Zhou X, Luan J, Wang J, Zheng S, Jiao Z, Dong C, Liaw PK. Developing novel high-temperature soft-magnetic B2-based multi-principal-element alloys with coherent body-centered-cubic nanoprecipitates. Acta Mater 2024;266:119686. https://doi.org/10.1016/j.actamat.2024.119686.

[21] Borkar T, Gwalani B, Choudhuri D, Mikler CV, Yannetta CJ, Chen X, Ramanujan RV, Styles MJ, Gibson MA, Banerjee R. A combinatorial assessment of AlxCrCuFeNi2 (0 < x < 1.5) complex concentrated alloys: microstructure, microhardness, and magnetic properties. Acta Mater 2016;116:63–76. https://doi.org/10.1016/j.actamat.2016.06.025.

[22] Noce RD, Gomes ODM, de Magalhães SD, Wolf W, Guimarães RB, De Castro AC, Barthem VMTS. Magnetic properties of Fe–Cu alloys prepared by pulsed electrodeposition. J Appl Phys 2009;106:93907. https://doi.org/10.1063/1.3253725.

[23] Kneller EF. Magnetic and structural properties of metastable FeCu solid solutions. J Appl Phys 1964;35:2210. https://doi.org/10.1063/1.1702819.

[24] Awadhi MA, Egilmez M, Abuzaid W, Alami AH. Magnetic properties and non-fermi liquid behaviour in mechanically alloyed FeCu. J Alloys Compd 2021;890:161812. https://doi.org/10.1016/j.jallcom.2021.161812.

[25] Alami AH, Hawili AA. Synthesis, characterization and applications of FeCu alloys. Appl. Surf. Sci. Adv. 2020;1:100027. https://doi.org/10.1016/j.apsadv.2020.100027.

[26] Chow GM, Ambrose T, John Xiao Q, Twiggl ME, Barall S, Ervinl AM, Qadril SB, Fengl CR. Chemical preparation and properties of nanocrystalline FeCu alloy and composite powders. Nanostruct Mater 1992;1:361–8. https://doi.org/10.1016/0965-9773(92)90086-D.

[27] Chien CL, Liou SH. Magnetic properties of FeCu solid solutions. Phys Rev B 1986; 33:3247–50. https://doi.org/10.1103/PhysRevB.33.3247.

[28] Kim WR, Bang GB, Park JH, Lee TW, Lee B, Yang S, Kim G, Lee K, Kim HG. Microstructural study on a Fe-10Cu alloy fabricated by selective laser melting for defect-free process optimization based on the energy density. J Mater Res Technol 2020;9:12834–9. https://doi.org/10.1016/j.jmrt.2020.09.051.

[29] Wang M, Yang Q, Jiang Y, Li Z, Xiao Z, Gong S, Wang Y, Guo C, Wei H. Effects of Fe content on microstructure and properties of Cu–Fe alloy. Trans Nonferrous Metals Soc China 2021;31:3039–49. https://doi.org/10.1016/S1003-6326(21)65713-8.

[30] Liu S, Jie J, Guo Z, Yue S, Li T. A comprehensive investigation on microstructure and magnetic properties of immiscible Cu-Fe alloys with variation of Fe content. Mater Chem Phys 2019;238:121909. https://doi.org/10.1016/j.matchemphys.2019.121909.

[31] Suryanarayana C, Ivanov E, Boldyrev VV. The science and technology of mechanical alloying. Mater Sci Eng, A 2001;304–306:151–8. https://doi.org/10.1016/S0921-5093(00)01465-9.

[32] Chaudhary V, Sai Kiran Kumar Yadav NM, Mantri SA, Dasari S, Jagetia A, Ramanujan RV, Banerjee R. Additive manufacturing of functionally graded Co–Fe and Ni–Fe magnetic materials. J Alloys Compd 2020;823:153817. https://doi.org/10.1016/j.jallcom.2020.153817.

[33] Rodgers JL, Nicewander WA. Thirteen ways to look at the correlation coefficient. Am Statistician 1988;42:59–66. https://doi.org/10.1080/00031305.1988.10475524.

[34] Binary Alloy Phase Diagrams. In: Okamoto H, Schlesinger ME, Mueller EM, editors. Alloy phase diagrams. ASM International; 2016. https://doi.org/10.31399/asm.hb.v03.a0006247.

[35] Terohid SAA, Heidari S, Jafari A, Asgary S. Effect of growth time on structural, morphological and electrical properties of tungsten oxide nanowire. Appl Phys A 2018;124:567. https://doi.org/10.1007/s00339-018-1955-0.

[36] Tiller WA. Preferred growth direction of metals. JOM (J Occup Med) 1957;9: 847–55. https://doi.org/10.1007/BF03397928.

[37] Haghdadi N, Cizek P, Hodgson PD, He Y, Sun B, Jonas JJ, Rohrer GS, Beladi H. New insights into the interface characteristics of a duplex stainless steel subjected to accelerated ferrite-to-austenite transformation. J Mater Sci 2020;55:5322–39. https://doi.org/10.1007/s10853-020-04358-3.

[38] Srinivasarao B, Oh-Ishi K, Ohkubo T, Hono K. Bimodally grained high-strength Fe fabricated by mechanical alloying and spark plasma sintering. Acta Mater 2009;57: 3277–86. https://doi.org/10.1016/j.actamat.2009.03.034.

[39] Zhao M, Zhang P, Xu J, Ye W, Yin S, Zhao J, Qiao Y, Yan Y. Optimization of microstructure and tensile properties for a 13Cr-1W ODS steel prepared by mechanical alloying and spark plasma sintering using pre-alloyed powder. Mater Char 2024;207:113581. https://doi.org/10.1016/j.matchar.2023.113581.

[40] Pasebani S, Charit I, Butt DP, Cole JI, Wu Y, Burns J. Sintering behavior of lanthana-bearing nanostructured ferritic steel consolidated via spark plasma sintering. Adv Eng Mater 2016;18:324–32. https://doi.org/10.1002/adem.201500294.

[41] Keller C, Tabalaiev K, Marnier G, Noudem J, Sauvage X, Hug E. Influence of spark plasma sintering conditions on the sintering and functional properties of an ultra-fine grained 316L stainless steel obtained from ball-milled powder. Mater Sci Eng, A 2016;665:125–34. https://doi.org/10.1016/j.msea.2016.04.039.

[42] Li J, Wen M, Gong Y, Zhao Z. Effects of the addition of NbC on the performance of copper-based composites by spark plasma sintering. Bull Mater Sci 2024;47:145. https://doi.org/10.1007/s12034-024-03208-1.

[43] Le GM, Godfrey A, Hansen N. Structure and strength of aluminum with sub-micrometer/micrometer grain size prepared by spark plasma sintering. Mater Des 2013;49:360–7. https://doi.org/10.1016/j.matdes.2013.01.018.

[44] Tan LP, Padhy SP, Tsakadze Z, Chaudhary V, Ramanujan RV. Accelerated property evaluation of Ni–Co materials libraries produced by multiple processing techniques. J Mater Res Technol 2022;20:4186–96. https://doi.org/10.1016/j.jmrt.2022.08.152.

[45] Tsakadze Z, Tan LP, Davidson KP, Gorsse S, Chaudhary V, Ramanujan RV. Accelerated multi-property discovery of promising Fe-Si-Al magnetic alloys. Materialia 2024;36:102168. https://doi.org/10.1016/j.mtla.2024.102168.

[46] Herzer G. Grain size dependence of coercivity and permeability in nanocrystalline ferromagnets. IEEE Trans Magn 1990;26:1397–402.

[47] Shi S, Liu X, Huang S, Zhang Y, Li H, Xu H, Li Z, Bai G, Li Z, Zhang X. Optimization of magnetic domain structure and soft magnetic properties of FeCoNiGd medium-entropy alloys by gadolinium addition. J Alloys Compd 2024;970:172654. https://doi.org/10.1016/j.jallcom.2023.172654.

[48] Zhou C, Jiang H, Liu C, Yan B, Yan P. Microstructure features of high performance soft magnetic alloy Fe-3 wt.% Si prepared by metal injection molding. Mater Chem Phys 2021;273:125068. https://doi.org/10.1016/j.matchemphys.2021.125068.

[49] Samsonov GV. Electrical and magnetic properties of the elements. In: Handbook of the physicochemical properties of elements. Boston: Springer; 1968. p. 314–73.

[50] Han K, Walsh RP, Ishmaku A, Toplosky V, Brandao L, Embury JD. High strength and high electrical conductivity bulk Cu. Philos Mag 2004;84:3705–16. https://doi.org/10.1080/14786430412331293496.

[51] Fiorillo F, Bertotti G, Appino C, Pasquale M. Soft magnetic materials. John Wiley & Sons, Inc.; 2016. p. 1–42.